Golden Single-atomic-site Platinum Electrocatalysts

Paul N. Duchesne,[†] Z.Y. Li, [‡,#] Christopher P. Deming, [§,#] Victor Fung,[⊥,#] Xiaojing Zhao,[‖] Jun Yuan,[∇] Tom Regier,[O] Ali Aldalbahi,[⁋] Zainab Almarhoon, [⁋] Shaowei Chen, [§] De-en Jiang,[⊥] Nanfeng Zheng, [‖] and Peng Zhang*,[†]

[†] Department of Chemistry, Dalhousie University, 6274 Coburg Road, Halifax, NS, Canada

[‡] Nanoscale Physics Research Laboratory, School of Physics & Astronomy, University of Birmingham, Birmingham, B15 2TT, UK

[§] Department of Chemistry and Biochemistry, University of California, Santa Cruz, CA 95064, USA

[⊥] Department of Chemistry, University of California, Riverside, CA 92521, USA

[‖] State Key Laboratory for Physical Chemistry of Solid Surfaces, and Collaborative Innovation Center of Chemistry for Energy Materials, College of Chemistry and Chemical Engineering, Xiamen University, Xiamen 361005, China

[∇] Department of Physics, University of York, York, YO10 5DD, UK

[O] Canadian Light Source, Saskatoon, SK, Canada

[⁋] Department of Chemistry, College of Science, King Saud University, P.O. Box 2455, Riyadh 11451, Kingdom of Saudi Arabia

[*] Corresponding author, Email: peng.zhang@dal.ca

[#] Equally contributing second authors

Keywords: gold, platinum, colloidal synthesis, single-atomic site, alloy bonding, electrocatalysis, formic acid oxidation

25   **Abstract**

26   Bimetallic nanoparticles with tailored structure constitute a desirable model system for catalysts,

27   as crucial factors such as geometric and electronic effects can be readily controlled by tailoring

28   the structure and alloy bonding of the catalytic site. Herein, we report a facile colloidal method to

29   prepare a series of platinum-gold (PtAu) nanoparticles with tailored surface structures and

30   particle diameters on the order of 7 nm. Samples with low Pt content, particularly Pt_4Au_{96},

31   exhibited unprecedented electrocatalytic activity for the oxidation of formic acid. A high forward

32   current density of 3.77 $A \cdot mg_{Pt}^{-1}$ was observed for Pt_4Au_{96}, a value two orders of magnitude

33   greater than those observed for core-shell-structured $Pt_{78}Au_{22}$ and a commercial Pt nanocatalyst.

34   Extensive structural characterization and theoretical DFT simulations of the best-performing

35   catalysts revealed densely packed single-atom Pt surface sites surrounded by Au atoms,

36   suggesting that their superior catalytic activity and selectivity could be attributed to the unique

37   structural and alloy bonding properties of these single-atomic-site catalysts.

38

39

40   Platinum (Pt) has a long history of use in catalysis, due primarily to its high activity in a

41   wide range of chemical reactions.[1] However, it faces major obstacles in some reactions,

42   including the problem of carbon monoxide (CO) poisoning in the formic acid oxidation (FAO)

43   reaction.[2] Due to the very strong binding affinity of CO at Pt surfaces, exposure to even small

44   quantities of CO can gradually poison (*i.e.*, deactivate) a Pt catalyst.[3] In recent years, it has

45   become common to alloy Pt with other metals in order to modify its catalytic properties;[4–7] thus,

46   it seems reasonable this approach could also be used to address the issue of CO poisoning and

47   enhance the performance of such Pt catalysts.[8,9] Recent advances in nanoparticle synthesis have

48   allowed for the preparation of bimetallic nanocatalysts with increasingly well-defined alloy

49   structures.[10–13] An important quality of these bimetallic nanoparticles is that the interaction

50   between atoms of different metals at the nanoparticle surface can result in significantly enhanced

51   catalytic activity due to both geometric and electronic effects.[14–16] By definition, these alloy

52   interactions occur at the boundaries between domains of the two metals; thus, any catalytic

53   enhancement effect should also be maximized by increasing the degree of intermetallic mixing at

54   the nanoparticle surface.[16] A very interesting and little-researched limit to this mixing is found in

55   single-Pt-site catalysis in an alloy nanoparticle system, wherein distinct geometric and electronic

56   effects set it apart from other phase-segregated surface nanostructures via the so-called

57   "ensemble effect" theory.[17–21]

58   Herein is presented a series of colloidal bimetallic PtAu nanoparticles, obtained via a

59   facile solution-phase synthesis, that feature stable single-atomic Pt catalytic sites with high FAO

60   activity. Electrocatalytic measurements reveal a remarkable enhancement in activity that is

61   highly dependent on the PtAu composition of the sample. Characterization of such materials is

62   very challenging, as Pt and Au have nearly identical atomic numbers. Nonetheless, we

63   demonstrate that convincing conclusions can be achieved through the use of several

64   complementary techniques, including X-ray absorption spectroscopy (XAS), X-ray

65   photoelectron spectroscopy (XPS), energy dispersive X-ray spectroscopy (EDX), high-angle

66   annular dark-field scanning transmission electron microscopy (HAADF-STEM), and

67   electrochemical measurements, with each offering its own insights into the structure of the

68   subject material. The results of this structural characterization, together with density functional

69   theory (DFT) modeling, demonstrate that it is not only elemental composition that dictates the

70 electrocatalytic activity of the PtAu nanoparticles, but that the local bonding environment of

71 single-atomic-site Pt surface atoms plays the most critical role.

72   The bimetallic PtAu nanoparticles used in this study were prepared from stock solutions

73 of Pt and Au chloride precursor salts using a colloidal synthetic method adapted from that of

74 Chen *et al.*[16] This synthetic procedure and a complete set of the PtAu samples with

75 systematically varied compositions from 4% Pt to 96% Pt are provided in Supplementary Fig. 1.

76 An illustration of nanoparticle formation from ions in solution is shown in Fig. 1a. Of particular

77 importance was the replacement of the CO reducing agent/co-ligand (used in the original

78 synthesis) with ethylene glycol (EG), such that the PtAu nanoparticles were prepared in a CO-

79 free environment. Following synthesis, these nanoparticles were deposited onto a carbon powder

80 support material in preparation for catalytic activity testing. Transmission electron microscopy

81 (TEM) was employed to confirm successful sample preparation (see Supplementary Fig. 2), and

82 inductively coupled plasma optical emission spectroscopy (ICP-OES) was used to measure

83 relative elemental compositions and mass loadings (see Supplementary Table 1). TEM results

84 confirmed a high degree of nanoparticle dispersion and uniformity, with observed mean particle

85 diameters of *ca.* 7 nm for all samples, and ICP-OES measurements revealed an average mass

86 loading of 11 ± 2 wt% for the carbon-supported samples. The measured elemental compositions

87 from ICP-OES (*i.e.*, $Pt_{78}Au_{22}$, $Pt_{53}Au_{47}$, $Pt_{17}Au_{83}$, Pt_7Au_{93}, and Pt_4Au_{96}) corresponded closely to

88 the nominal concentrations of Pt and Au used during synthesis, and are hereafter used to

89 distinguish between PtAu samples.

90   CV analysis yielded a very interesting result regarding the specific electrocatalytic

91 activities of the PtAu nanoparticles. As can be seen from the magnitude of the Pt-mass-

92 normalized current peaks at *ca.* 0.6 V_{RHE} in the anodic sweeps (see Fig. 1b), the highest activities

93 were observed for those samples containing the least Pt. The most active sample, Pt_4Au_{96},

94 exhibited activity greater than that of the commercial Pt/C catalyst and least-active PtAu

95 nanoparticle sample by up to two orders of magnitude (*i.e.*, 126 times greater than $Pt_{78}Au_{22}$, and

96 90 times greater than Pt/C). A strong correlation was observed between low FAO peak currents

97 and the presence of a significant peak at *ca.* 0.85 V_{RHE} in the CV plot. This secondary peak arises

98 from the electrochemical oxidation of adsorbed CO molecules, which are well known to poison

99 the surface of Pt and suppress its catalytic activity.[22] The absence of such a peak in the CV plots

100 of those PtAu nanoparticles containing the least Pt suggests that resistance to CO poisoning may

4

101   play a significant role in their enhanced catalytic activity. It should be noted that characterization

102   of pure Au nanoparticles, prepared according to the same protocol, revealed no measureable

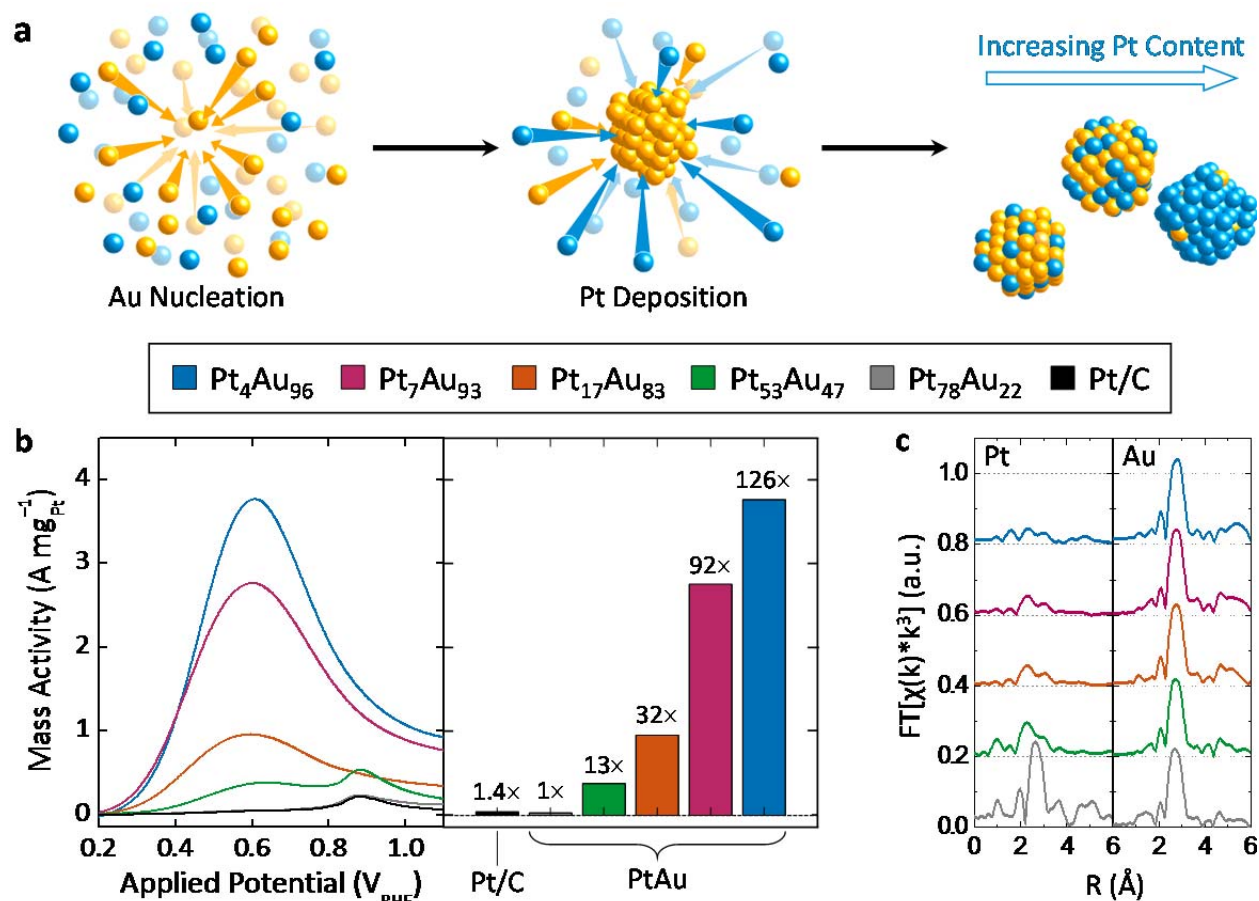103   activity in the FAO reaction (see Supplementary Fig. 3).

104

Fig. 1 | Synthesis, reactivity and EXAFS of catalysts. a, Illustration of nanoparticle formation via reduction of solvated ions. **b**, Pt mass-normalized anodic sweeps obtained from PtAu nanoparticle catalysts in electrolyte containing 0.1 M concentrations of both $HClO_4$ and $HCOOH$, with peak currents graphed for comparison. The data acquired from a commercial Pt/C catalyst is included to provide additional context. **c**, Plotted FT-EXAFS spectra obtained from Pt and Au L_3-edge absorption spectra of PtAu nanoparticles, illustrating the drastic under-coordination of Pt atoms in low-Pt-content samples such as Pt_7Au_{93} and Pt_4Au_{96}.

113   In order to gain a structural perspective on this activity enhancement, FT-EXAFS

114   analysis was performed on the PtAu nanoparticles at the Pt and Au L_3 absorption edges, shown

115   in Fig. 1c. Detailed information regarding the local Pt and Au bonding environments in each

116   sample was obtained by fitting these spectra (see Supplementary Fig. 4), resulting in the

117   structural parameter values shown in Table 1. Observed trends in coordination number and bond

118   length values are also presented graphically in Supplementary Fig. 5. While the scattering paths

involving Pt and Au atoms were too similar to produce separable peaks in the FT-EXAFS

spectrum (see Supplementary Fig. 6 for a topographical illustration), this similarity made it

possible to treat scattering from both Pt and Au as a single path (denoted Pt–M and Au–M for the

Pt and Au L_3-edges, respectively). Analysis of the resulting bond lengths suggested that Pt atoms

in Pt_7Au_{93} and Pt_4Au_{96}, the most highly active PtAu samples, were present almost exclusively as

single-atom sites surrounded by atoms of Au. This observation is based on the close agreement

between the measured Pt–M bond lengths (2.82 Å) and the expected bimetallic bond length of

2.822 Å for a homogenous PtAu alloy, as calculated from experimental Pt–Pt and Au–Au bond

lengths in pure Pt and Au nanoparticles (see Supplementary Table 2). Further evidence for the

single-atom structure of Pt in these two samples is provided via HAADF-STEM,

electrochemistry and XPS valence band analyses. It is notable that a similar Pt–M bond distance

was also observed for $Pt_{17}Au_{83}$; however, its Pt–M coordination number (CN) is identical to that

of the core-shell structured nanoparticles ($Pt_{53}Au_{47}$ and $Pt_{78}Au_{22}$) and considerably higher than

the single-atom Pt samples. These results indicate that $Pt_{17}Au_{83}$ exhibits a mixed structure

containing both single-atom and few-atom Pt cluster regions, with more of them located within

the core of the nanoparticle. Additional support for this conclusion is provided by the particularly

large Debye-Waller coefficient (σ^2) value obtained for $Pt_{17}Au_{83}$, indicating that there is greater

variation among the Pt–M bond lengths due to significant contributions from both Pt–Pt and Pt–

Au bonds. Further evidence will also be provided in the electrochemical and valence band

studies.

Table 1 | Structural parameter values for PtAu nanoparticles.

Sample	Pt–M				Au–M			
	CN (atoms)	R (Å)	σ^2 (10^{-3} Å^2)	ΔE_0 (eV)	CN (atoms)	R (Å)	σ^2 (10^{-3} Å^2)	ΔE_0 (eV)
$Pt_{100}Au_0$	11.1(5)	2.772(1)	2.1(2)	3.9(4)	-----	-----	-----	-----
$Pt_{78}Au_{22}$	9(1)	2.776(4)	2.6(6)	3(1)	12(1)	2.839(4)	4.3(6)	0(1)
$Pt_{53}Au_{47}$	9(2)	2.776(8)	3(2)	2(1)	12.1(9)	2.851(3)	4.2(4)	2.3(7)
$Pt_{17}Au_{83}$	9(1)	2.818(5)	8(1)	2.8(8)	11.6(9)	2.861(3)	3.6(4)	2.6(7)
Pt_7Au_{93}	7.4(9)	2.813(5)	6(1)	2.6(8)	12(1)	2.862(4)	3.4(5)	2(1)
Pt_4Au_{96}	5(2)	2.82(2)	4(3)	3(3)	11.0(8)	2.871(2)	3.1(3)	3.4(6)
Pt_0Au_{100}	-----	-----	-----	-----	12.0(4)	2.872(1)	3.4(2)	2.7(3)

140 EXAFS analysis of local CNs revealed that Pt atoms were under-coordinated in the PtAu

141 nanoparticles, especially those bearing highly active single-atom sites. CNs for the Pt–M

142 scattering path ranged from 9 nearest neighbours in Pt$_{78}$Au$_{22}$ to just 5 in Pt$_4$Au$_{96}$, standing in

143 stark contrast with the CN of 11 observed for pure Pt nanoparticles synthesized using the same

144 method. Combined with Au–M CNs on the order of 11 to 12 nearest neighbours, this evidence

145 strongly suggests an Au-core/PtAu shell nanoparticle structure, with Pt predominantly located at

146 surface sites. Furthermore, Pt concentrations measured using surface-sensitive X-ray

147 photoelectron spectroscopy (XPS) were consistently greater than those obtained using bulk-

148 sensitive ICP-OES (see Supplementary Fig. 7), providing convincing evidence of Pt surface-

149 enrichment in all PtAu nanoparticle samples. The very low CNs observed for Pt$_7$Au$_{93}$ and

150 Pt$_4$Au$_{96}$ (7 and 5, respectively) further indicate that Pt should be predominantly found on the

151 particle surface with high-level surface roughness, including edge and corner sites.[12] X-ray

152 absorption near edge structure (XANES) analysis of samples (see Supplementary Fig. 8) further

153 confirmed the metallic nature of both Pt and Au in these nanoparticles, and provided support for

154 the presence of single-atom Pt sites via a positive binding energy shift and increased white line

155 breadth (both indicative of increasingly isolated Pt atoms[23]). This high degree of direct Pt–Au

156 interaction was also observed in the XPS data, which featured a negative shift of the Pt 4f

157 electron binding energies of Pt$_{17}$Au$_{83}$ and Pt$_4$Au$_{96}$ (as was shown in Supplementary Fig. 7). In

158 contrast to the extensive Pt–Au mixing in those samples with a low Pt content, Pt$_{53}$Au$_{47}$ and

159 Pt$_{78}$Au$_{22}$ exhibited predominantly Pt–Pt bonding, reflecting their more complete Au-core/Pt-shell

160 structures.

161 The emerging picture of these nanoparticles as containing Pt preferentially located at the

162 surface of Au cores is consistent with real space imaging of these nanoparticles using atomic

163 resolution high angle annular dark field scanning transmission electron microscopy (HAADF-

164 STEM) and elemental imaging using spatially resolved energy dispersive X-ray (EDX)

165 spectroscopy (see Fig. 2a-c). In order to prevent beam damage to these nanoparticles, electron

166 beam intensity was minimized during EDX spectroscopy measurements, which resulted in low

167 X-ray counting statistics; nonetheless, there is strong evidence for Au signal originating
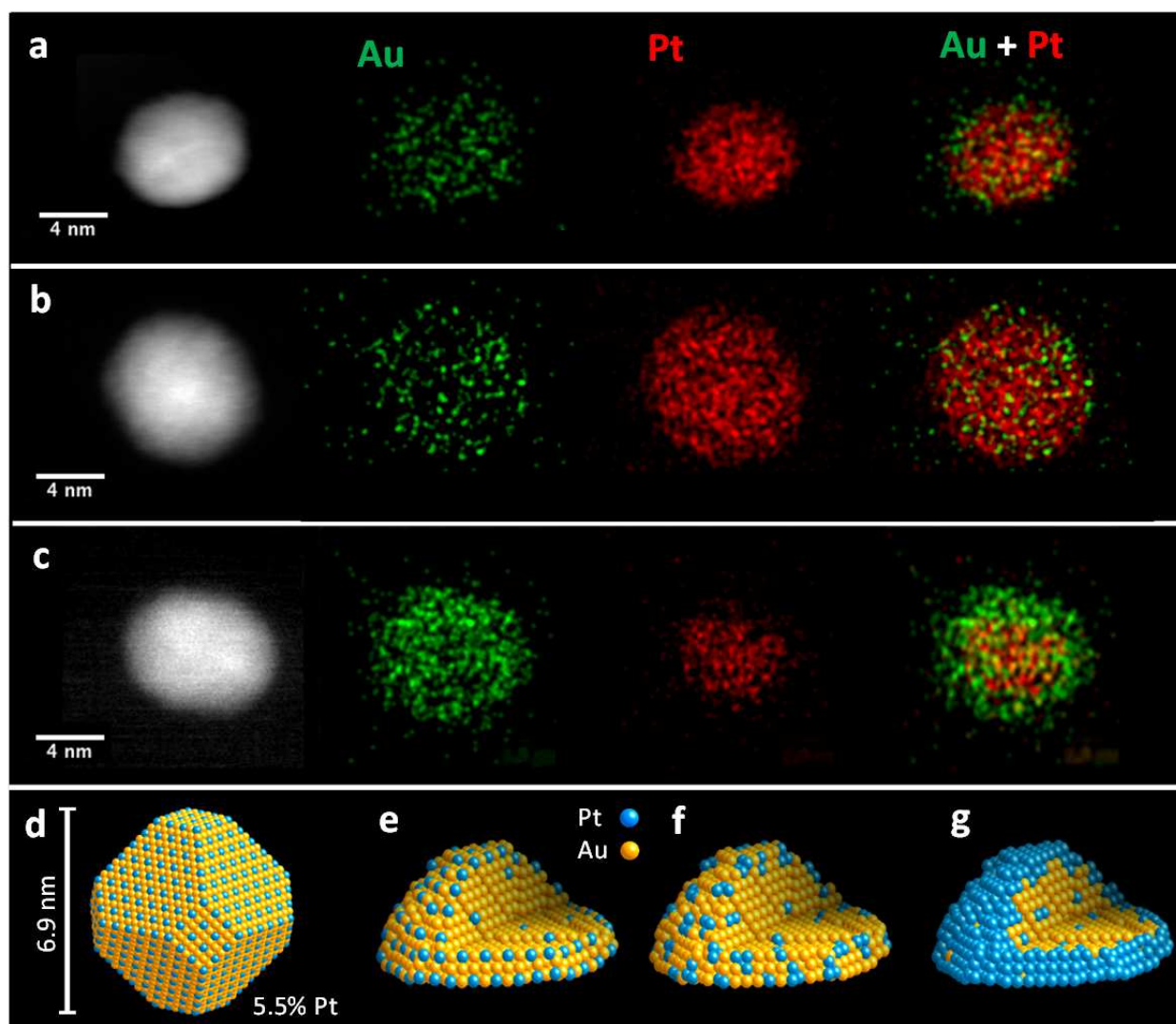
169
170

Fig. 2 | HAADF-STEM images and structural models. a, **b**, **c**, STEM/EDX mapping images of individual particles from Pt_4Au_{96} and Pt_7Au_{93} single-atom Pt, and $Pt_{78}Au_{22}$ core-shell samples, respectively. **d**, Structural model of an ideal, truncated octahedral nanoparticle with optimal single-atomic site coverage. Though strictly not representative of the nanoparticles synthesized herein, this model provides a reasonable estimate of the upper concentration limit for such single-atom Pt sites. **e**, **f**, **g**, Models depicting the proposed evolution of PtAu surface structures from single-atom Pt sites to few-atom Pt clusters to a complete Pt shell, respectively, as a result of increased Pt content.

mainly from the cores of nanoparticles, with the Pt signal being more diffuse and slightly enhanced at the particle edges. This effect can also be illustrated by comparing the overlay EDX maps of representative particles shown in Fig.2a-c. It is noteworthy that similar control over surface structure generally requires two or more sequential steps during synthesis, as Pt and Au are capable of forming homogeneous alloys.[23–26] The ability to achieve these complex surface

184   morphologies in a single reaction step likely stems from a combination of factors, including

185   sequential reduction (due to the more negative reduction potential of Au relative to Pt) and

186   preferential coordination of stabilizing amine ligands to surface Pt sites rather than Au sites.[27,28]

187   The significantly greater adsorption energy of the oleylamine ligand molecules at surface Pt sites

188   can contribute to the preferential Au-core/Pt-shell structure of the PtAu nanoparticles, as it

189   results in greater stabilization and limits further deposition of Au atoms, thereby resulting in a Pt-

190   enriched surface.

191   The observation of a Pt-rich surface is consistent with a single-atom Pt surface structure.

192   For an ideal truncated octahedral nanoparticle (see Fig. 2d), maximum surface coverage by

193   single-atomic sites (*i.e.*, with no co-adjacent Pt atoms) is achieved with a Pt content of 5.5%.

194   While atomic-scale HAADF-STEM images suggest that the PtAu nanoparticles synthesized

195   herein are predominantly polycrystalline, this single-crystalline estimate serves as a reasonable

196   upper concentration limit at which exclusively single-atom Pt sites are able to exist, and suggests

197   that Pt_4Au_{96} and Pt_7Au_{93} could reasonably exhibit such a surface morphology.

198   Based on the available information, the PtAu samples can now be categorized in terms of

199   their surface structure: Au with single-atom Pt sites (Pt_7Au_{93} and Pt_4Au_{96}), Au with single-atom

200   and few-atom Pt sites ($Pt_{17}Au_{83}$), and Au-core/Pt-shell ($Pt_{78}Au_{22}$ and $Pt_{53}Au_{47}$). This gradual

201   change from single-atomic to near-complete shell coverage in these PtAu/C nanocatalysts is

202   illustrated in Fig. 2e-g. Additional support for the proposed surface structures of the

203   nanoparticles can be found in the detailed analysis of their electrocatalytic performance

204   presented in Fig. 3. The disappearing peak at *ca.* 0.85 V_{RHE} in Fig. 1b is more clearly shown in

205   the first-derivative plots of Pt mass activity in Fig. 3a. Such peak intensity was completely absent

206   in both the Pt_7Au_{93} and Pt_4Au_{96} samples (as is more clearly illustrated in Supplementary Fig. 9),

207   and was markedly reduced in $Pt_{17}Au_{83}$. These electrochemical results offer another piece of

208   evidence for the Pt single-atom structure in Pt_7Au_{93} and Pt_4Au_{96}. As is illustrated in Fig. 3c, the

209   existence of adjacent Pt surface sites will produce a CO poisoning peak in the first derivative

210   voltammogram, whereas the single-atom Pt geometry of the catalyst surface will encourage the

211   CO_2 formation via the dehydrogenation mechanism. Moreover, the small CO first derivative

212   peak for $Pt_{17}Au_{83}$ in Fig. 3a illustrates the existence of some smaller, cluster-like Pt domains in

213   this sample. Fig. 3b shows that a similar trend in specific activity is observed when normalizing

214   FAO anodic sweep voltammograms by the electrochemically active surface area (ECSA) of Pt,

215 indicating again that the observed increase in activity was not simply due to an increased

216 proportion of Pt surface sites in those samples with lower Pt content. Both Pt_7Au_{93} and Pt_4Au_{96}

217 exhibited very similar peak intensities when the anodic sweeps were normalized by the

218 combined ECSAs of Pt and Au, suggesting that they shared a similar surface structure in addition

219 to their mutual resistance to CO poisoning. Finally, normalization of electrocatalytic

220 performance by total metal catalyst mass resulted in a trade-off between reduced surface

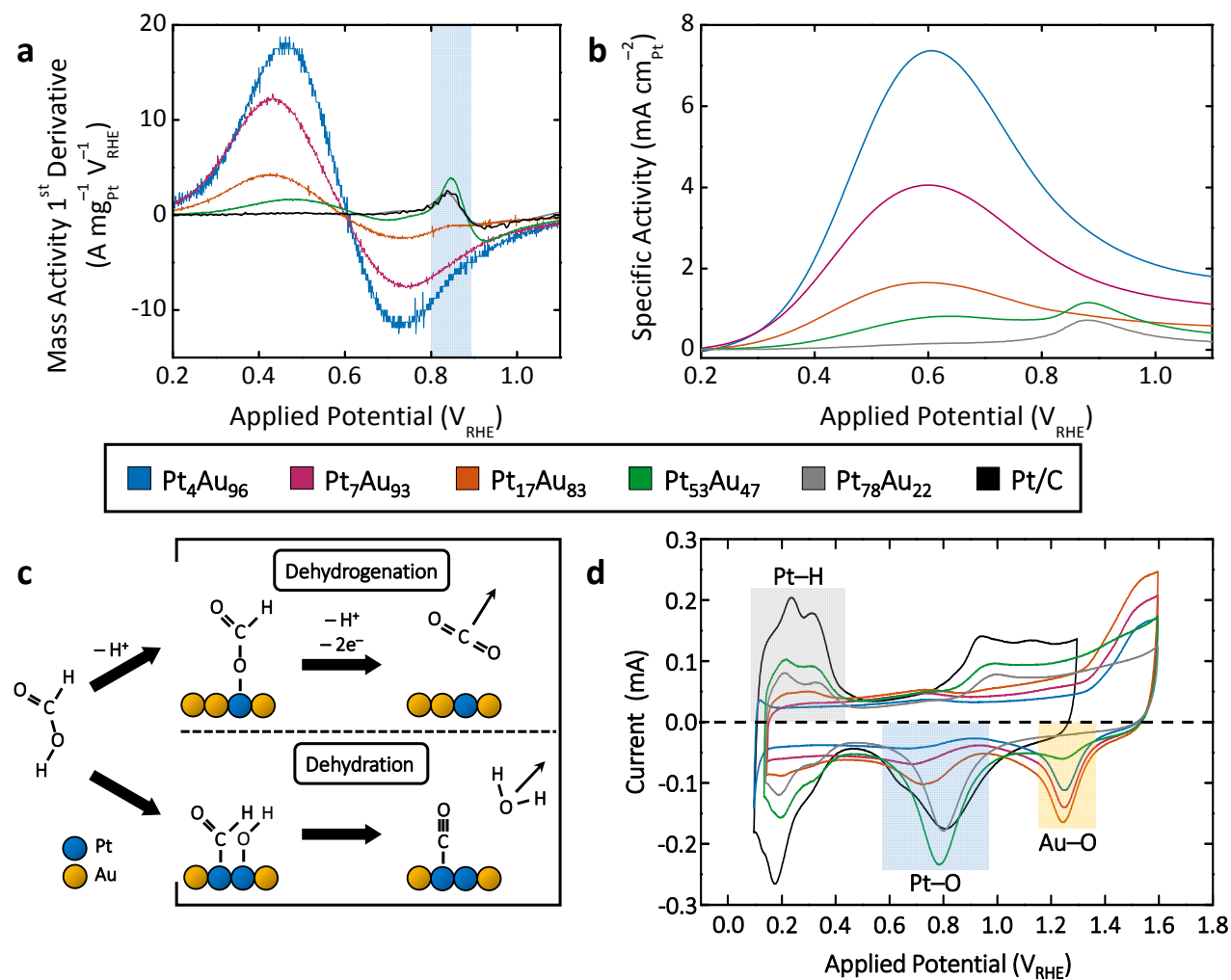221 poisoning by CO and the number of available Pt catalytic sites (see Supplementary Fig. 10).

222

Fig. 3 | Further electrochemical analysis. a, First-derivative of Pt mass-normalized FAO voltammograms presented in Fig. 1a. The blue box highlights the sensitivity of the first-derivative peak at *ca.* 0.85 V_{RHE} to the Pt surface structure. **b**, FAO anodic sweep voltammograms obtained from PtAu nanoparticle and commercial Pt/C catalyst samples, as normalized by the electrochemically active surface area of Pt. These voltammograms were also obtained using a sweep rate of 10 $mV \cdot s^{-1}$ and an electrolyte containing 0.1 M concentrations of both $HClO_4$ and HCOOH. **c**, Schematic illustration of the dehydrogenation and dehydration mechanisms of FAO reactions on PtAu surfaces. **d**, Cyclic voltammograms from PtAu nanocatalysts (shown at full amplitude) and commercial Pt nanocatalysts (shown at half amplitude to facilitate comparison) acquired in 0.1 M $HClO_4$ with a sweep rate of 100 $mV \cdot s^{-1}$.

232

233   This structure is experimentally supported by the behaviour of distinct Au–O adlayer

234   formation on the exposed Au surfaces, as revealed by CV measurements under non-catalytic

235   conditions (see Fig. 3d). Regions of interest include the positive Pt–H desorption peaks

236   highlighted from *ca.* 0.1 to 0.4 V_{RHE}, and the negative Pt–O and Au–O adlayer removal peaks

237   highlighted from 0.55 to 0.95 V_{RHE} and from 1.15 to 1.35 V_{RHE}, respectively. As expected from

238   the relative compositions, the areas of the Pt–O and Au–O adlayer removal peaks revealed a

239   gradual transition from a pure Pt surface in $Pt_{78}Au_{22}$ (indicative of its Au-core/Pt-shell structure)

240   to the predominantly Au surface decorated with Pt in Pt_4Au_{96}. In addition to a steady reduction

241   of Pt–H peak area, a significant negative shift of the Pt–O adlayer removal peak was observed

242   with decreasing Pt content; this shift reached a maximum of *ca.* 0.1 V_{RHE} in Pt_4Au_{96}, revealing

243   markedly strengthened Pt–O adsorption, likely due to the increasingly lowered coordination

244   numbers of Pt atoms in these samples. This observation provides strong evidence for the

245   thorough mixing of Pt and Au at the surface of samples with low Pt content, resulting in a

246   relatively even distribution of Pt across the predominantly Au surface. The less-drastic shift of

247   the Au–O adlayer desorption peak relative to that of Pt–O can be explained by the fact that any

248   charge transfer effects involve up to 9 Au atoms per Pt atom, depending on the relative

249   composition of the sample.

250   Given that CO poisoning has a drastic impact on the measured activity of Pt-based FAO

251   catalysts, DFT calculations were performed to study the adsorption properties of CO at single-

252   atom, few-atom, and pure Pt surfaces (see Fig. 4a-c). The (111) surface is selected in our DFT

253   calculations since the (111) sites are the most abundant surface sites in regular colloidal Au and

254   Pt nanoparticles. Multiple adsorption sites for CO exist at pure and few-atom Pt surfaces (in

255   order of increasing adsorption energy: apical, bridging, hcp hollow, and fcc hollow), whereas

256   only a single site (apical) was found to be significant for the single-atom Pt surface. The results

257   of these calculations indicate that CO adsorption is weakened at all adsorption sites on both few-

258   atom and single-atom Pt surfaces relative to bulk Pt (see Fig. 4d and Supplementary Table 3).

259   Adsorption energies of CO at apical sites, for example, are reduced from −1.268 eV on bulk Pt to

260   −1.063 and −1.032 eV on few-atom and single-atom surfaces, respectively. This finding is in line

261   with the observed enhancement in FAO activity, rationalized via a weakening of the typically

262   too-strong CO adsorption on Pt (as per the Sabatier Principal).[29,30] While this weakened CO

263   adsorption is consistent with the observed activity enhancement, however, it is generally

264   recognized that the availability of adjacent adsorption sites also makes a significant contribution

265   to FAO activity.[7] It is worthwhile to note that the PtAu nanoparticles also show significant

266   retention of activity as shown by both chronoamperometric measurements performed at 0.55

267   V_{RHE} and repeated cycling between 0.1 and 1.1 V_{RHE} (Supplementary Fig. 11). These results

268   further indicate the fairly good stability of the alloy-based single-atom catalysts, with the latter

269   demonstrating that high activity (> 70% of the initial value) can be retained even after 1,500

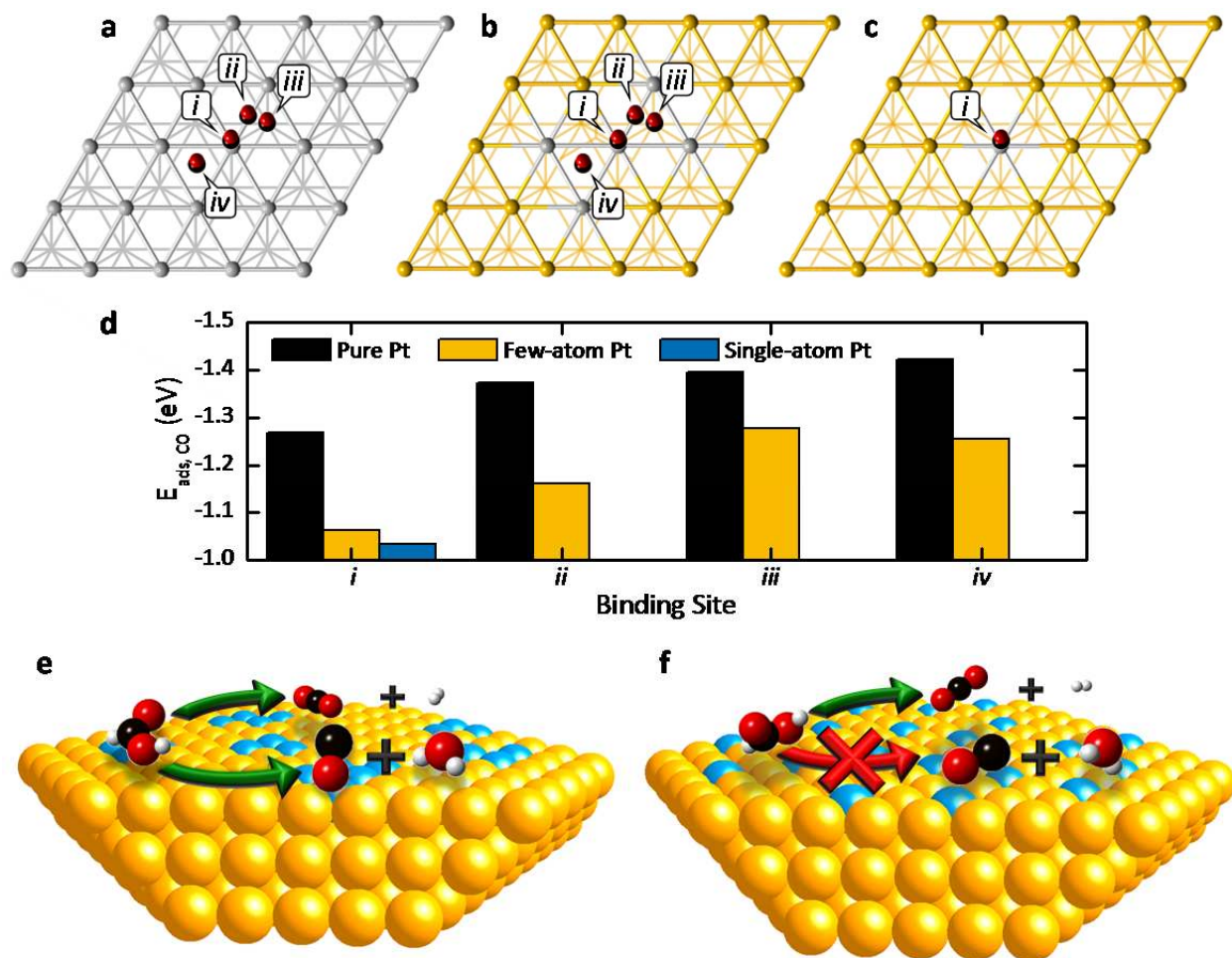270   successive rounds of potential cycling.

271

272 **Fig. 4 | DFT-calculated binding of CO at PtAu surfaces. a**, **b**, **c**, Illustration of CO adsorption modes on model (111)
273 lattices of pure, few-atom, and single-atomic Pt surfaces, respectively, including apical (*i*), bridging (*ii*), hcp hollow
274 (*iii*), and fcc hollow (*iv*) coordination sites. **d**, Calculated adsorption energies for the indicated CO adsorption sites.
275 **e**, **f**, Predominant FAO reaction pathways on few-atom (or greater) and single-atom Pt surfaces, highlighting the
276 selectivity achieved via the ensemble effect.
277

278   While a number of possible pathways exist for the oxidation of formic acid at Pt surfaces,

279   the dehydrogenation and dehydration pathways tend to predominate, overall (see Fig. 4e).[30] The

280   former pathway is responsible for the majority of the observed FAO activity of Pt, the latter is a

281   major concern, as it leads to the formation of adsorbed CO species at Pt sites and blocks them

282   from participating in future reaction steps. Due to its large impact on catalytic activity, surface

283   morphology also plays a large role in determining which of these two reaction pathways will

284   predominate. Both DFT calculations[31] and experimental evidence[32] support this observation,

285   indicating that only one Pt adsorption site is required for formic acid dehydrogenation, whereas

286   the indirect dehydration pathway requires a greater number of adjacent atoms. This so-called

287   "ensemble effect" strongly discourages the detrimental indirect reaction, leaving the direct

288   dehydrogenation reaction as the primary reaction pathway (see Fig. **Error! Reference source**

289   **not found.**4f). Thus, the formation of isolated single-atom catalytic sites can be linked to the

290   remarkable activity increases observed in these PtAu nanocatalysts.

291   Valence band analysis was also performed on the PtAu/C nanocatalyst using both DFT

292   density of states (DOS) calculations and XPS measurements to better understand the electronic

293   effect of alloy formation on catalytic activity. The DFT DOS results in Fig. 5a predict a drastic

294   reduction of intensity near the Fermi level (*i.e.*, 0 eV) for the single-atomic PtAu surface relative

295   to the pure Pt surface. Tellingly, in the XPS valence band measurements shown in Fig. 5b-e, the

296   near-Fermi level DOS (*i.e.*, –2 to 0 eV) is also found to be very sensitive to the local structural

297   environment of Pt. The two samples bearing single-atom Pt sites, Pt_4Au_{96} and Pt_7Au_{93}, show the

298   lowest DOS intensity in the near-Fermi level region, being virtually identical to the pure Au

299   surface. In contrast, a pronounced increase in DOS intensity near the Fermi level is observed for

300   the few-atom-cluster Pt sample, $Pt_{17}Au_{83}$. Finally, when a more complete Pt shell is formed at the

301   Au nanoparticle surface in $Pt_{53}Au_{47}$, the near-Fermi level DOS becomes higher still and its

302   intensity begins to approach that of the pure Pt surface.

303   The aforementioned results indicate that samples containing larger amounts of Pt

304   demonstrate much more pronounced Pt character in their valence bands, resulting in increased

305   DOS intensities near the Fermi level. For single-atom Pt surfaces, however, no such Pt–Pt

306   bonding exists and the overall DOS is determined by the predominant Au–Au bonding. Thus, the

307   low DOS intensities observed near the Fermi level of single-atom Pt surfaces arises from the

308   large number of Au atoms relative to Pt. When Pt–Pt bonds begin to appear, as occurs in the few-
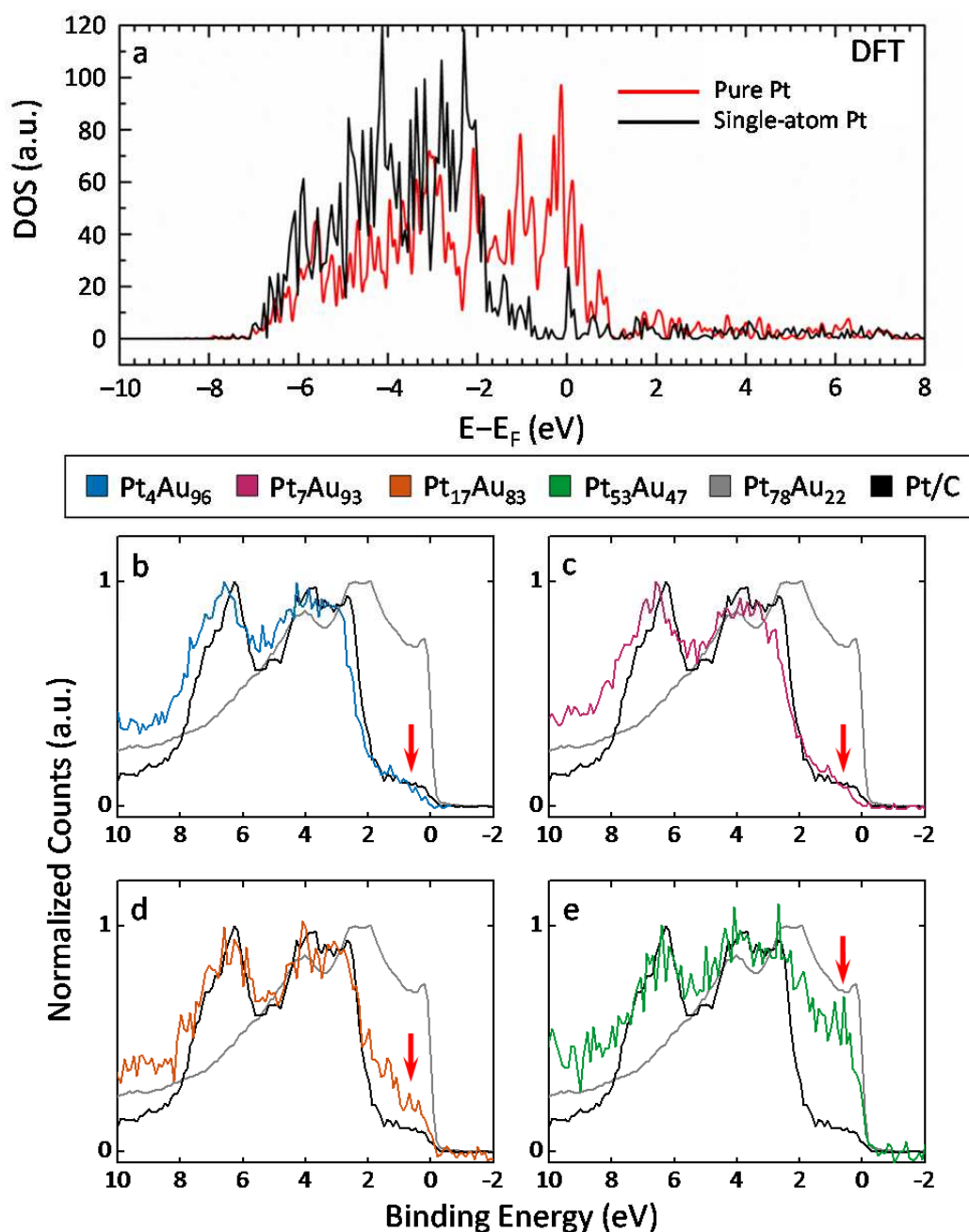
309

310

Fig. 5 | Calculated and experimental DOS. a, Calculated DFT density of states (DOS) plots corresponding to the

pure and single-atom Pt surfaces used to calculate CO adsorption energies in Fig. 4a-d. **b**, **c**, **d**, **e**, XPS valence band

spectra of Pt_4Au_{96}, Pt_7Au_{93}, $Pt_{17}Au_{83}$, and, $Pt_{53}Au_{47}$ samples compared against those of Pt and Au foil references.

Red arrows indicate the near-Fermi level region, wherein samples containing single-atom Pt sites show

considerable difference from those containing few-atom cluster and core-shell Pt surfaces.

316

317   atom Pt clusters of $Pt_{17}Au_{83}$, the DOS intensity of the near-Fermi level increases

318   considerably. These results are in good agreement with previous observations that DOS intensity

319   near the Fermi level is determined primarily by chemical bonding between like nearest neighbor

320   atoms.[33] This means that the identical near-Fermi level DOS intensities observed for Pt_4Au_{96},

321   Pt_7Au_{93}, and the bulk Au reference prove, again, the single-atomic Pt structure for these two

322   PtAu nanoparticle samples. Furthermore, the valence band structure of PtAu nanoparticle

323   samples is also closely linked to their catalytic performance. Due to relativistic effects, the d-

324   orbitals of Au are higher in energy, and the valence s-orbital lower, than would typically be

325   expected, resulting in a shift of electron density from the former to the latter. As a result, Au

326   atoms are less able to accept σ-donated electrons and engage in π back-donation to adsorbed CO

327   molecules, weakening CO adsorption energies on these surfaces as was shown previously in Fig.

328   4.

329   In conclusion, bimetallic PtAu nanoparticles with extraordinary electrocatalytic FAO

330   activity have been synthesized using a facile and easily tuneable colloidal method. By

331   employing a comprehensive suite of structural characterization techniques, these PtAu

332   nanocatalysts were identified as having distinct Au-core/Pt-shell, few-atom Pt cluster, or single-

333   atom Pt surface structures, dictated by their relative elemental compositions. Structural

334   characterization revealed a high surface density of low-coordinate, single-atom Pt sites in

335   Pt_7Au_{93} and Pt_4Au_{96}, which, according to the ensemble effect theory, prevented these catalysts

336   from self-poisoning via CO generation at their surfaces. Thus, the observed orders-of-magnitude

337   increase in Pt mass-normalized FAO activity for the best-performing PtAu nanocatalyst (single-

338   atomic Pt_4Au_{96}) relative to the poorest (core-shell $Pt_{78}Au_{22}$ and commercial Pt) is readily

339   explained in terms of surface structure and alloy bonding. DFT calculations further supported

340   these results by revealing weakened adsorption of CO to few-atom and single-atom Pt surfaces

341   as a result of both electronic effects arising from Pt-Au bonding interactions and the formation of

342   discrete single-atom Pt catalytic sites (*i.e.*, the ensemble effect). Unlike many other published

343   syntheses, only a single-step colloidal method was required to achieve a high degree of control

344   over surface structure and alloy bonding, and a very high surface packing density of single-atom

345   catalytic sites up to 7% can be achieved. As a result, the excellent electrocatalytic activity of

346   these PtAu nanoparticles represents remarkable progress in the development of single-atomic-

site Pt catalysis, with their exceptional selectivity enabling the use of highly active Pt to perform

reactions typically prohibited by CO poisoning.

Methods

References

1.   Chen, A. & Holt-Hindle, P. Platinum-based nanostructured materials: Synthesis, properties, and applications. *Chem. Rev.* **110,** 3767–3804 (2010).

2.   Hunt, S. T. *et al.* Self-assembly of noble metal monolayers on transition metal carbide nanoparticle catalysts. *Science* **352,** 974–978 (2016).

3.   Yu, Y., Wang, X. & Lim, K. H. A DFT study on the adsorption of formic acid and its oxidized intermediates on (100) facets of Pt, Au, monolayer and decorated Pt@Au surfaces. *Catal. Letters* **141,** 1872–1882 (2011).

4.   Wang, X., He, B., Hu, Z., Zeng, Z. & Han, S. Current advances in precious metal core–shell catalyst design. *Sci. Technol. Adv. Mater.* **15,** 043502 (2014).

5.   Liu, X., Wang, D. & Li, Y. Synthesis and catalytic properties of bimetallic nanomaterials with various architectures. *Nano Today* **7,** 448–466 (2012).

6.   Liu, X., Wang, D. & Li, Y. Bimetallic nanocrystals: Liquid-phase synthesis and catalytic applications. *Adv. Mater.* **23,** 1044–1060 (2011).

7.   Jiang, K., Zhang, H.-X., Zou, S. & Cai, W.-B. Electrocatalysis of formic acid on palladium and platinum surfaces : from fundamental mechanisms to fuel cell applications. *Phys. Chem. Chem. Phys.* **16,** 20360–20376 (2014).

8.   Liu, J. *et al.* Tackling CO poisoning with single atom alloy catalysts. *J. Am. Chem. Soc.* **138,** 6396–6399 (2016).

9.   Yuge, K., Koyama, Y., Kuwabara, A. & Tanaka, I. Surface design of alloy protection against CO-poisoning from first principles. *J. Phys. Condens. Matter* **26,** 355006 (2014).

10.   Habrioux, A. *et al.* Structural and electrochemical studies of Au-Pt nanoalloys. *Phys. Chem. Chem. Phys.* **11,** 3573–3579 (2009).

11.   Ji, X. *et al.* Nanocrystalline intermetallics on mesoporous carbon for direct formic acid fuel cell anodes. *Nat. Chem.* **2,** 286–293 (2010).

12.   Zhang, H., Watanabe, T., Okumura, M., Haruta, M. & Toshima, N. Catalytically highly active top gold atom on palladium nanocluster. *Nat. Mater.* **11,** 49–52 (2012).

13.   Guo, S. *et al.* Nanocatalyst superior to Pt for oxygen reduction reactions: The case of

382   core/shell Ag(Au)/CuPd nanoparticles. *J. Am. Chem. Soc.* **136,** 15026–15033 (2014).

383   14.   Yang, X.-F. *et al.* Single-atom catalysts: A new frontier in heterogeneous catalysis. *Acc.*
384   *Chem. Res.* **46,** 1740–1748 (2013).

385   15.   Qiao, B. *et al.* Single-atom catalysis of CO oxidation using $Pt_1/FeOx$. *Nat. Chem.* **3,** 634–
386   641 (2011).

387   16.   Chen, G. *et al.* Interfacial effects in iron-nickel hydroxide-platinum nanoparticles
388   enhance catalytic oxidation. *Science* **344,** 495–499 (2014).

389   17.   Roy, A. *et al.* Enhanced catalytic activity of Ag/Rh bimetallic nanomaterial: Evidence of
390   an ensemble effect. *J. Phys. Chem. C* **120,** 5457–5467 (2016).

391   18.   Prinz, J. *et al.* Ensemble effect evidenced by CO adsorption on the 3-fold PdGa surfaces.
392   *J. Phys. Chem. C* **118,** 12260–12265 (2014).

393   19.   Zaera, F., Gellman, J. A. & Somorjai, G. A. Surface science studies of catalysis:
394   Classification of reactions. *Acc. Chem. Res.* **19,** 24–31 (1986).

395   20.   Ruff, M., Takehiro, N., Liu, P., Nørskov, J. K. & Behm, R. J. Size-specific chemistry on
396   bimetallic surfaces: A combined experimental and theoretical study. *ChemPhysChem* **8,** 2068–
397   2071 (2007).

398   21.   Sachtler, W. M. H. Chemisorption complexes on alloy surfaces. *Catal. Rev. - Sci. Eng.*
399   **14,** 193–210 (1976).

400   22.   Stevanović, S. *et al.* Insight into the effect of Sn on CO and formic acid oxidation at PtSn
401   catalysts. *J. Phys. Chem. C* **118,** 278–289 (2014).

402   23.   Duchesne, P. N. & Zhang, P. Element-specific analysis of the growth mechanism, local
403   structure, and electronic properties of Pt clusters formed on Ag nanoparticle surfaces. *J. Phys.*
404   *Chem. C* **118,** 21714–21721 (2014).

405   24.   Yu, Y., Hu, Y., Liu, X., Deng, W. & Wang, X. The study of Pt@Au electrocatalyst based
406   on Cu underpotential deposition and Pt redox replacement. *Electrochim. Acta* **54,** 3092–3097
407   (2009).

408   25.   Kim, J., Jung, C., Rhee, C. K. & Lim, T. Electrocatalytic oxidation of formic acid and
409   methanol on Pt deposits on Au (111). *Langmuir* **23,** 10831–10836 (2007).

410   26.   Luo, J. *et al.* Phase properties of carbon-supported gold-platinum nanoparticles with
411   different bimetallic compositions. *Chem. Mater.* **17,** 3086–3091 (2005).

412   27.   Atkins, P. & de Paula, J. in *Physical Chemistry* 1005–1006 (W.H. Freeman and
413   Company, 2006).

414   28.   Wu, B. & Zheng, N. Surface and interface control of noble metal nanocrystals for
415   catalytic and electrocatalytic applications. *Nano Today* **8,** 168–197 (2013).

416   29.   Bligaard, T. *et al.* The Brønsted–Evans–Polanyi relation and the volcano curve in
417   heterogeneous catalysis. *J. Catal.* **224,** 206–217 (2004).

418   30.   Zhong, W. & Zhang, D. New insight into the CO formation mechanism during formic
419   acid oxidation on Pt(111). *Catal. Commun.* **29,** 82–86 (2012).

420   31.   Neurock, M., Janik, M. & Wieckowski, A. A first principles comparison of the

mechanism and site requirements for the electrocatalytic oxidation of methanol and formic acid over Pt. *Faraday Discuss.* **140,** 363–378 (2009).

32.   Cuesta, A., Escudero, M., Lanova, B. & Baltruschat, H. Cyclic voltammetry, FTIRS, and DEMS study of the electrooxidation of carbon monoxide, formic acid, and methanol on cyanide-modified Pt (111) electrodes. *Langmuir* **25,** 6500–6507 (2009).

33.   Mason, M. Electronic structure of supported small metal clusters. *Phys. Rev. B* **27,** 748–762 (1983).

34.   Schneider, C. A., Rasband, W. S. & Eliceiri, K. W. NIH Image to ImageJ: 25 years of image analysis. *Nat. Methods* **9,** 671–675 (2012).

35.   Kraft, S., Stümpel, J., Becker, P. & Kuetgens, U. High resolution X-ray absorption spectroscopy with absolute energy calibration for the determination of absorption edge energies. *Rev. Sci. Instrum.* **67,** 681–687 (1996).

36.   Bearden, J. A. X-ray wavelengths. *Rev. Mod. Phys.* **39,** 78–124 (1967).

37.   Ressler, T. WinXAS: A program for X-ray absorption spectroscopy data analysis under MS-Windows. *J. Synchrotron Radiat.* **5,** 118–122 (1998).

38.   Ankudinov, A. L., Ravel, B., Rehr, J. J. & Conradson, S. D. Real-space multiple-scattering calculation and interpretation of X-ray-absorption near-edge structure. *Phys. Rev. B* **58,** 7565–7576 (1998).

39.   Wagner, C. D. in *Practical Surface Analysis* (eds. Briggs, D. & Seah, M. P.) 635–638 (1990).

40.   Naumkin, A. V., Kraut-Vass, A., Gaarenstroom, S. W. & Powell, C. J. NIST X-ray photoelectron spectroscopy database. (2012). at <http://srdata.nist.gov/xps/>

41.   Luo, S., Zhao, Y. & Truhlar, D. G. Improved CO adsorption energies, site preferences, and surface formation energies from a meta-generalized gradient approximation exchange–correlation functional, M06-L. *J. Phys. Chem. Lett.* **3,** 2975–2979 (2012).

Acknowledgements

462

Author contributions

464 P.N.D synthesized all samples, conducted the XAS experiments and analysis, performed some of

465 the electrochemical and TEM studies, and wrote the manuscript. P.Z. designed the project,

466 coordinated the whole process of the work, and supervised P.N.D. to conduct this research.

467 Z.Y.L. and J.Y. performed the HAADF-STEM measurements and image analysis. C.P.D.

468 performed the electrochemical experiments under the supervision of S.C. V.F. conducted the

469 DFT calculations under the supervision of D.J. X.Z contributed to the TEM measurements under

470 the supervision of N.Z. A.A. and Z.A. also contributed to part of the TEM measurements. T.R.

471 performed some of the XPS measurements at the Canadian Light Source.

472

Competing Financial Interests

474 The authors declare no competing financial interests.

475

Additional information

477 Supplementary information is available for this paper at https://doi.org/10.1038

478

Methods

480 **Materials.** Dihydrogen hexachloroplatinate ($H_2PtCl_6 \cdot 6H_2O$, 99.9 %), hydrogen tetrachloroaurate

481 ($HAuCl_4 \cdot 3H_2O$, 99.9 %), ethylene glycol (EG, 99+ %), and HiSPEC 3000 carbon-supported Pt

482 catalyst (Pt/C, $\leq$ 500 ppm impurities) were purchased from Alfa Aesar. Oleylamine (OAm, C18-

483 content 80-90 %) and formic acid (HCOOH, 99 %) were purchased from Acros Organics.

484 Vulcan XC-72 carbon powder was purchased from Cabot. Nafion® 117 Solution (Nafion, 5 %)

485 and n-butylamine ($BuNH_2$, 99.5 %) were purchased from Sigma Aldrich. Perchloric acid

486 ($HClO_4$, 70 %) was purchased from Fisher Scientific. Ethanol used in cyclic voltammetry

487   experiments (EtOH, 96 %) was purchased from J.T. Baker. All reagents and solvents were used

488   as received, without further purification.

489   **Synthesis of PtAu Nanoparticles.** PtAu nanoparticles were prepared from stock solutions of Pt

490   and Au chloride precursor salts, with nominal compositions of 10, 25, 50, and 75 atom% Pt

491   being selected by controlling the ratio of precursors used. In a typical synthesis, 72.5 mg

492    $H_2PtCl_6 \cdot 6H_2O$ and 55.1 mg $HAuCl_4 \cdot 3H_2O$ were each dissolved in 70 mL of OAm through a

493   combination of ultrasonication and manual mixing to obtain metal precursor stock solutions.

494   Appropriate volumes of these Pt and Au stock solutions (prepared in OAm) were then added to a

495   100 mL round-bottom flask to give the desired Pt-to-Au ratio with a total volume of 20 mL. An

496   additional 20 mL of EG was then added while mixing vigorously using a magnetic stirrer. The

497   resulting mixture was subsequently bubbled with $N_{2(g)}$ for several minutes in order to remove

498   dissolved $O_{2(g)}$ from solution. Each mixture was then placed in a 180 ºC oil bath, sealed, and

499   allowed to react for 1 h. Once the reaction was complete, flask was removed from heat and

500   allowed to cool to room temperature while still sealed under a $N_{2(g)}$ atmosphere. Due to the large

501   excess of reducing agents employed in this reaction (OAm and EG, also functioning as solvents),

502   all Pt^{4+} and Au^{3+} species can reasonably be assumed to have been reduced to a zero-valent state.

503   In order to purify the product nanoparticles, each sample was divided amongst several 30 mL

504   polypropylene centrifuge tubes. The nanoparticles were precipitated via addition of two to three

505   volume equivalents of EtOH, and then isolated by centrifuging the resulting suspension (at 6,000

506   RPM for 5 min) and decanting the supernatant. The precipitated nanoparticles were then

507   redispersed in hexanes via brief ultrasonication and shaking before being again precipitated and

508   centrifuged. After this second centrifugation cycle, the purified nanoparticles were redispersed in

509   hexanes and centrifuged once more to remove any insoluble material.

510   **Deposition of PtAu Nanoparticles onto XC-72 Carbon Powder.** Following purification, the

511   nanoparticle samples were deposited onto an XC-72 carbon powder support material via ligand

512   exchange-induced destabilization. A nanoparticle loading of 20 wt% (by total mass of Pt and Au)

513   was selected in order to allow for better comparison with the commercial Pt/C catalyst (HiSPEC

514   3000, 20 wt% Pt) used as a reference material for electrocatalytic testing. For each sample, four

515   mass equivalents of XC-72 powder (assuming a theoretical yield of 100 % for each nanoparticle

516   sample) were added to 15 mL of $BuNH_2$ and thoroughly dispersed via ultrasonication. Each

517   purified nanoparticle sample was then precipitated using EtOH and isolated via centrifugation

518   and decantation. The isolated nanoparticle material was redispersed and extracted from the

519   centrifuge tube using ultrasonication and successive aliquots of the previously prepared XC-

520   72/BuNH$_2$ suspension. This final mixture was then allowed to stir magnetically for 24 h in order

521   to allow the ligand exchange and nanoparticle deposition to occur gradually. Finally, the post-

522   deposition PtAu nanoparticle materials were isolated once more via EtOH addition and

523   centrifugation (at 12,000 RPM for 20 min) and allowed to dry in air.

524   **Transmission Electron Microscopy.** Bright field TEM imaging of the samples was performed

525   both prior to and following deposition onto the XC-72 carbon support. In preparation for

526   analysis, each sample was dispersed in *ca.* 200 μL EtOH via sonication and drop-cast onto

527   Formvar-coated copper TEM grids. Unsupported PtAu nanoparticle samples were imaged using

528   a JEOL JEM-2100F transmission electron microscope operated at a 200 kV accelerating voltage.

529   PtAu nanoparticle samples supported on XC-72 carbon powder were imaged using a Tecnai F-30

530   transmission electron microscope operated at a 300 kV accelerating voltage. Size distributions

531   and mean particle diameters of the nanoparticles were measured and calculated using

532   MacBiophotonics ImageJ software[34] using several representative images from each sample.

533   HAADF and EDX mapping measurements were performed at the University of Birmingham

534   (UK) using a JEOL 2100F scanning transmission electron microscope with a CEOS aberration-

535   corrector. A JEOL annular dark field detector was used for HAADF imaging and a Bruker

536   XFlash 4030 silicon drift detector was used for EDX mapping of the PtAu nanoparticle samples.

537   During the EDX mapping, the HAADF-STEM images were monitored to check for possible

538   beam-induced structure changes of the atomic structure. EDX data presented are from only those

539   nanoparticles that did not show any visible structural changes.

540   **X-ray Absorption Spectroscopy.** XAS measurements were performed using the Sector 20-BM

541   beamline of the Advanced Photon Source at Argonne National Laboratory in Argonne, IL. The

542   end-station was equipped with a double-crystal Si(111) monochromator for wavelength

543   selection, which was detuned to 80 % in order to help reject higher harmonics of the desired

544   energy; a toroidal focusing mirror was also employed to further enhance harmonic rejection.

545   Gas-ionization detectors were used to measure the absorption spectra of Pt and Au foil reference

546   materials; however, data acquisition from the bimetallic nanoparticles was complicated by

547   overlap between the spectra obtained at the Pt and Au L$_3$-edges (occurring at 11,562.76 eV and

548   11,919.70 eV, respectively[35]). This challenge was addressed by employing a 12-element Ge

549 fluorescence detector to collect data from the bimetallic PtAu nanoparticles. Although there also

550 exists overlap between the Pt and Au L_α emission peaks centered at 9,442.3 eV and 9,713.3 eV,

551 repectively[36]), nearly all of the interfering signal could be filtered out by excluding the

552 overlapping energy region between the two (as depicted in Supplementary Fig. 12). While

553 excluding this region also resulted in a reduction of fluorescence intensity, the loss was largely

554 offset by the greater sensitivity of the fluorescence detector relative to standard absorption

555 detectors. As a result, useable spectra were obtained for all samples through the use of this

556 method. In order to compensate for the greater amount of noise present in the fluorescence data,

557 PtAu nanoparticle samples were held at 90 ± 1 K during measurement in order to enhance

558 EXAFS signal intensity by supressing thermal vibrations in the material. Full details regarding

559 the data ranges ("k-range" and "R-range") used to obtain and fit the FT-EXAFS spectra are

560 presented in the Supporting Information (Supplementary Table 4). Data processing and fitting

561 were performed using WinXAS[37] and Analyzer v0.1 software, with scattering paths generated by

562 FEFF8[38]. S_0^2 values for Pt and Au (both equal to 0.93) were obtained by fitting a metallic

563 reference foil of same element. A bulk, homogeneous PtAu alloy structural model was used to

564 calculate the Pt–M and Au–M scattering paths used in FT-EXAFS fitting. A single metal-metal

565 scattering path was used in fitting the FT-EXAFS data because insufficient degrees of freedom

566 were available to include separate Pt and Au scattering paths; the Pt–M and Au–M fitting values

567 reported herein thus represent averages of the Pt–Pt/Pt–Au and Au–Au/Au–Pt contributions.

568 **X-ray Photoelectron Spectroscopy.** X-ray photoelectron spectroscopy (XPS) measurements

569 were performed at Canadian Light Source in Saskatoon, Canada, using an excitation energy of

570 3,000 eV at the SXRMB beamline and an excitation energy of 300 eV at the SGM beamline.

571 PtAu/C nanocatalyst samples were prepared by spreading the powder onto conductive, double-

572 sided carbon tape, which was then affixed to a copper sample holder. Many scans of each sample

573 were averaged together in order to obtain higher signal-to-noise ratios. Relative PtAu

574 compositions were determined from peak areas obtained by fitting the Pt and Au 4f peaks using

575 Au^0/Au^+ and Pt^0/Pt^{2+} contributions in conjunction with empirically derived atomic sensitivity

576 factors.[39] Splitting between $4f_{5/2}$ and $4f_{7/2}$ peaks was set based upon data obtained from the

577 NIST X-ray Photoelectron Spectroscopy Database.[40] Full-width at half-maximum values for the

578 $4f_{5/2}$ and $4f_{7/2}$ peaks within each contribution were correlated to be equal, and relative area ratios

579 were correlated such that area($4f_{7/2}$):area($4f_{5/2}$) = 4:3. XPS valence band spectra were collected

580   using an excitation energy of 3,000 eV and normalized by setting the valence band maximum

581   equal to unity.

582   **Cyclic Voltammetry.** Cyclic voltammetry was performed using a CHI 710 electrochemical

583   work station with a three-electrode setup, including a polished glassy carbon working electrode

584   (rotating disc electrode), a Ag/AgCl reference electrode, and a Pt sheet counter electrode. A

585   solution of 0.1 M perchloric acid was used as the supporting electrolyte, with the addition of 0.1

586   M formic acid during FAO activity measurements. Catalyst "ink" suspensions were prepared by

587   dispersing the carbon-supported PtAu material in EtOH via ultrasonication to obtain a final

588   catalyst concentration of 1 $\mu g \cdot \mu L^{-1}$. A volume of the Nafion solution equal to 1 % the volume of

589   added EtOH was then added and sonicated for a further 15 min to complete the preparation. For

590   ORR testing, 20 μL of the catalyst ink were drop-cast onto the glassy carbon electrode surface

591   and allowed to dry completely. A 3 μL volume of a diluted Nafion solution (20 % v/v in EtOH)

592   was then deposited onto the dried catalyst layer in order to help improve its physical stability and

593   electrical conductivity. The electrode surface was allowed to dry completely prior to

594   electrochemical testing. After purging the electrolyte solution with ultrahigh purity $N_{2(g)}$, CV

595   measurements were performed. Pt electrochemically active surface areas (ECSAs) were

596   calculated from the integrated region beneath the H-desorption peaks in each voltammograms,

597   whereas Au ECSAs were estimated from the integrated area of the Au–O adlayer removal peak.

598   **DFT Calculations.** DFT calculations were performed using Vienna *ab initio* package (VASP)

599   software. The revised Perdew-Burke-Erzerhof (RPBE) form of the generalized-gradient

600   approximation (GGA) was chosen for electron exchange and correlation in order to correct for

601   the over-binding of small molecules at transition metal surfaces observed using the standard

602   Perdew-Burke-Erzerhof approach. Although DFT-RPBE tends to overstabilize the hollow and

603   bridge sites over the atop site for CO adsorption on Pt(111), the adsorption energies on these

604   sites are quite close (within 0.10 eV) and in good agreement with the experimental value.[41] The

605   electron-core interaction was described using the projector-augmented wave method (PAW). A

606   kinetic energy cutoff of 450 eV was used for the planewaves, and the Brillouin zone was

607   sampled using a 3×3×1 Monkhorst-Pack scheme. The surface model slab was created using a

608   4×4 supercell of the Pt/Au unit cell, with four atomic layers and a 15 Å unit cell. Adsorption

609   energies were calculated using the following equation:

610    $$E_{ads} = E_{surface+adsorbate} - (E_{surface} + E_{adsorbate})$$

611   wherein the energy of the adsorbate, $E_{adsorbate}$, was computed by placing the CO adsorbate

612   molecule in a 10 Å wide cubic cell vacuum to prevent intermolecular interactions resulting from

613   the periodic boundary conditions.

614

615   **Data availability.**

616   The data supporting the results of this work are available from the authors on reasonable

617   requests.

618